Journal of Medical Robotics Research, Vol. 0, No. 0 (2022) 1–15


# Safer Motion Planning of Steerable Needles via a Shaft-to-Tissue Force Model

Michael Bentley[a], Caleb Rucker[b], Chakravarthy Reddy[c], Oren Salzman[d], and Alan Kuntz[a]

[a] *Robotics Center and Kahlert School of Computing, University of Utah, Salt Lake City, UT 84112, USA*
*E-mail: michael.bentley@utah.edu*

[b] *The Department of Mechanical, Aerospace, and Biomedical Engineering, University of Tennessee, Knoxville, TN 37996, USA*

[c] *Huntsman Cancer Institute and School of Medicine, University of Utah, Salt Lake City, UT 84112, USA*

[d] *Department of Computer Science, Technion - Israel Institute of Technology, Technion City, Haifa, 3200003, Israel*

Steerable needles are capable of accurately targeting difficult-to-reach clinical sites in the body. By bending around sensitive anatomical structures, steerable needles have the potential to reduce the invasiveness of many medical procedures. However, inserting these needles with curved trajectories increases the risk of tissue damage due to perpendicular forces exerted on the surrounding tissue by the needle's shaft, potentially resulting in lateral shearing through tissue. Such forces can cause significant tissue damage, negatively affecting patient outcomes. In this work, we derive a tissue and needle force model based on a Cosserat string formulation, which describes the normal forces and frictional forces along the shaft as a function of the planned needle path, friction model and parameters, and tip piercing force. We propose this new force model and associated cost function as a safer and more clinically relevant metric than those currently used in motion planning for steerable needles. We fit and validate our model through physical needle robot experiments in a gel phantom. We use this force model to define a bottleneck cost function for motion planning and evaluate it against the commonly used path-length cost function in hundreds of randomly generated 3-D environments. Plans generated with our force-based cost show a 62% reduction in the peak modeled tissue force with only a 0.07% increase in length on average compared to using the path-length cost in planning. Additionally, we demonstrate planning with our force-based cost function in a lung tumor biopsy scenario from a segmented computed tomography (CT) scan. By directly minimizing the modeled needle-to-tissue force, our method may reduce patient risk and improve medical outcomes from steerable needle interventions.

*Keywords*: Force modeling; robotic needle steering; bottleneck cost function; motion planning; continuum robots

## 1. Introduction

Bevel-tip steerable needles provide minimally invasive access to anatomical sites deep in the human body.[1–4] These needles leverage asymmetric tip forces to curve around anatomical obstacles during needle insertion, enabling accurate targeting of clinically relevant sites that are difficult or impossible to reach safely with traditional needles. The design trend has been to maximize the needle's curvature capability to increase reachability to many areas of the body in complex anatomy.[5,6] However, with an increase in curvature, the needle exerts more force on the surrounding tissue during deployment due to redirecting insertion forces.[2] With large tissue forces perpendicular to the needle (see Fig. 1) comes an increased potential of significant tissue damage, such as tissue compression or a shearing event,[2] where the needle shaft cuts sideways through the surrounding tissue, causing severe damage[4] (see Fig. 2).

Minimum path length and maximum clearance are the most commonly used cost functions in needle steering.[7–10] These cost functions are mainly intended to encourage planned motions that minimize some notion of tissue damage by piercing through less total tissue (path-length cost) or steering far from highly sensitive anatomical structures (obstacle-clearance cost).

In this work we instead develop an efficient model describing the forces from the needle's shaft on surrounding tissue for a given path. In our model, the force exerted by the needle on the surrounding tissue is a function of the puncture force at the needle's tip, the needle's shape through the tissue, and the friction between the needle's shaft and the surrounding tissue (see Fig. 1).

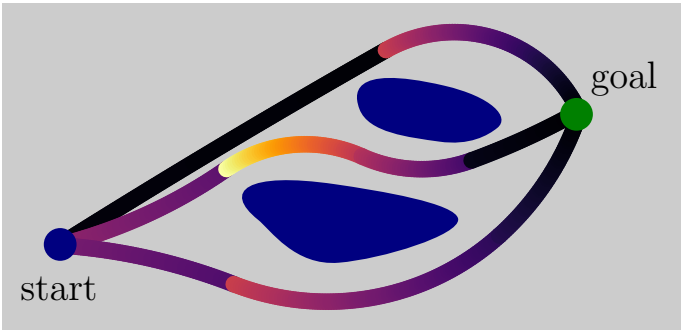


Fig. 1. A tissue normal force profile for three example paths using our new needle-to-tissue force and friction model. Darker colors indicate small forces and lighter colors indicate large forces. The upper and lower paths have similar lengths and maximum tissue forces. The middle path is 8.5% shorter but has 79% higher maximum normal force despite the top and middle paths having matching maximum curvatures. According to our model, the middle path has a higher probability of causing tissue damage than the other two paths.

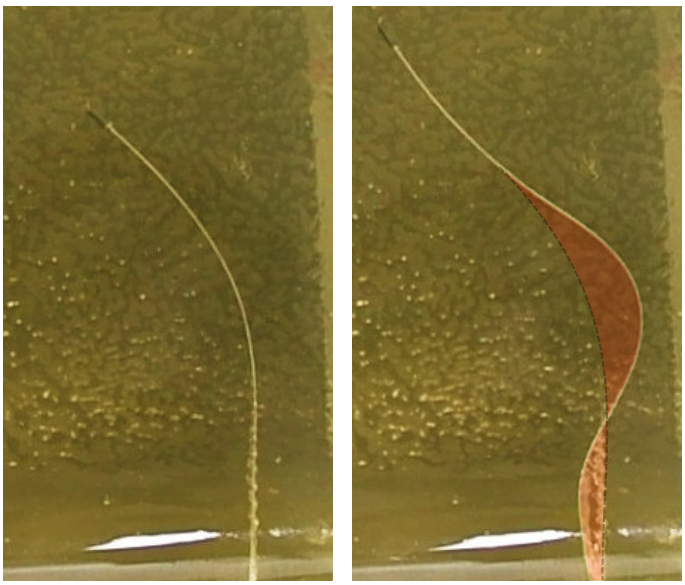

(a) (b)

Fig. 2. An example of a needle **(a)** before and **(b)** after significant shearing through gelatin. Shearing is lateral slicing by the needle shaft, caused by tissue fracturing due to excessive forces from the needle's shaft. In (b) we show a dotted line of the shape prior to shearing, and a red region showing the sheared area.

We develop a motion-planning cost function based on our force model. We assume that the magnitude of the tissue normal force is correlated with the probability of tissue damage, from tissue compression to shearing. We further assume that no shearing occurs below an unknown minimum force threshold. Thus, we incorporate the maximum tissue force along the shaft as a cost function during motion planning, to effectively push down the force peak below the minimum force threshold. This cost function, used in a suitable motion-planning algorithm, enables us to plan motions that reach clinically relevant targets while avoiding sensitive anatomical structures and directly minimizing the modeled normal force exerted upon the tissue by the needle shaft during insertion.

We propose this new clinically relevant force model and cost function as a replacement for currently used motion-planning cost functions with steerable needles. Notably, with this model, the tissue normal forces are dependent on the entire needle trajectory and cannot be determined locally in isolation. However, with a specified tip piercing force, we can compute the tissue normal forces in a single pass analytically, backward, starting at the needle's tip. As a key result, our model shows that neither path length nor maximum curvature along a path can accurately serve as a proxy metric for the tissue normal forces (see Fig. 1).

Our force-based cost function is an instance of a *bottleneck cost*, which has the full cost concentrated in a localized piece of the trajectory. In our case, the full cost is localized at the point of maximal tissue force. We demonstrate the use of this force-based cost with a modified motion-planning algorithm. This algorithm produces plans that achieve better costs, as computation time allows.

We provide the following contributions:

(1) a simple and efficient needle-to-tissue force and friction model;
(2) a new physically based and clinically relevant motion-planning cost function for needle steering based on our proposed model, and a motion-planning algorithm that leverages our force-based bottleneck cost function;
(3) two strategies for fitting our model parameters to experimental results without direct force measurements between the needle and tissue.

Our motion-planning experiments show that, compared to using the path-length cost, planning with our force cost generates paths with a 62% decrease in maximal force at the cost of only 0.07% higher path length on average.

## 2. Related Work

Due to their potential to reduce the invasiveness of many types of therapeutic and biopsy-based procedures, steerable needles have been proposed for use in the kidneys,[11] liver,[11] prostate,[12] brain,[13] and lung.[14] There exist many needle actuation designs, including beveled,[3] pre-bent,[13,15] passive flexure,[4,16] variable-length flexure,[17] active flexure,[18,19] fracture-directed inner stylet,[6] a programmable bevel,[20] and external magnetic actuation.[21–23] See van de Burg *et al.*[5] for a review on steerable needle designs. Most of these designs leverage an asymmetric tip, which causes them to curve in tissue as they are inserted from their base

outside of the tissue.[4,5]

Measuring and understanding the force interaction between the needle and tissue is important to minimizing tissue damage. Instrumented needle tips have measured the needle's piercing force to better understand the tip's interaction with different types of tissue and tissue boundaries.[24] Techniques have been used to decrease needle insertion force with barbs,[25] vibrations,[25,26] bidirectional rotation,[26] and slower insertion speeds.[27]

Many have attempted to model the force interaction between the needle shaft and surrounding tissue, modeling insertion forces, tissue deformation, needle deflection, and cutting forces.[1,28,29] These works primarily focus on finite-element simulations based on the full Cosserat-rod model and tissue mechanics.[30] Although these finite-element simulations are fast enough to enable real-time control of steerable needles, they are not efficient enough for motion planning since optimal motion planning searches the space of all possible valid trajectories, minimizing a cost. Instead, our force model is based on the Cosserat-string formulation, which enables a simpler analytically tractable model that can be incorporated into existing motion planners as the cost function with the goal of minimizing the tissue damage by the needle shaft, including compression and shearing.

Motion planning enables robots to plan trajectories that avoid obstacles while moving from some start state to a goal state. Sampling-based motion planning is a popular paradigm that leverages random sampling of configurations or controls to produce collision-free plans.[31] These include the Rapidly exploring Random Tree (RRT)[32] and Probabilistic Roadmap (PRM)[33] methods which incrementally construct a collision-free tree or graph.

Motion planning for steerable needles has been approached in a variety of ways. Pinzi *et al.*[10] present the Adaptive Hermite Fractal Tree algorithm, which leverages optimized geometric Hermite curves[34] combined with a fractal tree. Fu *et al.*[35] developed the Resolution-Complete Search (RCS) algorithm, and the resolution-optimal extension RCS*,[36] which provably finds the lowest-cost needle-steering plan within the resolution of a discretized needle-steering action space. Favaro *et al.*[37] adapt the Batch Informed Trees (BIT*) algorithm[38] combined with a path smoothing method in order to plan motions for a programmable bevel-tip needle. Patil *et al.*[7,39] built upon RRT to develop the Reachability-Guided RRT (RG-RRT) method for steerable needles. RG-RRT has been adapted in other work to plan motions for a three-stage lung tumor biopsy robot,[8] and to plan in pulmonary cost maps generated from medical imaging.[9] We build upon RG-RRT in this work, with a change that enables us to produce plans that achieve better costs, as computation time allows.

## 3. Method

We first derive our shaft-to-tissue force model, then we incorporate this force model as a bottleneck cost function in a motion-planning context.

### 3.1. *Shaft-to-Tissue Force Model*

We derive a model for the forces exerted by a flexible needle shaft traveling on a planned path through tissue. We model the needle as a Cosserat string,[30] which assumes infinite flexibility, and incorporate a kinetic friction model to derive tissue forces as a function of the needle's planned path through the tissue. This assumption becomes more accurate as the bending stiffness of the needle decreases, relative to the tissue modulus, a prominent design trend.[4,6]

#### 3.1.1. *Model Assumptions*

As needles become thinner and more flexible, the forces required to keep the needle bent in a static curved shape become negligible. As the needle is pushed through tissue, the piercing force $\boldsymbol{F}_p$ must be transmitted from an insertion force $\boldsymbol{F}_{\text{ins}}$ at the base of the needle along the shaft to the needle's tip. We assume that kinetic friction is the dominant force along the shaft and comes from the combination of compression from surrounding tissue and the needle pushing against the tissue along curves. The friction and normal forces are coupled in a way similar to the well-known capstan equation.[40] Therefore, we model the needle inside the tissue as an ideal Cosserat string, which assumes that (i) the flexural rigidity is negligible, and (ii) the internal force vector is always tangent to the needle's path.[30,41]

Conventionally, a Cosserat string is assumed to only carry tension force (since an ideal string will buckle under any compressive force). However, we assume that compressive force can be carried without buckling because the surrounding tissue will constrain the needle and prevent buckling, even for very low stiffness needles. The presented model is otherwise identical to a classical Cosserat string.

#### 3.1.2. *Needle Equilibrium*

In this model, the needle is characterized by its centerline curve in space $\boldsymbol{p}(s) \in \mathbb{R}^3$ as a function of the parameter $s \in [0, L]$, where $s$ is the arc length along the needle path of length $L$. The derivative of $\boldsymbol{p}(s)$ with respect to $s$, denoted as $\dot{\boldsymbol{p}}(s)$, is a unit vector tangent to $\boldsymbol{p}(s)$ pointing toward the robot's tip.

Along the needle's path, the tissue exerts a distributed force on the needle shaft which can be decomposed into two components, as seen in Fig. 3: one parallel to the needle, $\boldsymbol{f}_f(s) = -f_f(s)\dot{\boldsymbol{p}}(s)$, representing friction; and one perpendicular to the needle, $\boldsymbol{f}_\perp(s)$, representing the net normal force from tissue. The force balance on a small needle section of length $ds$ is then

$$-\boldsymbol{n}(s+ds) + \boldsymbol{n}(s) + \boldsymbol{f}_\perp(s)ds - f_f(s)\dot{\boldsymbol{p}}(s)ds = 0,$$

where $\boldsymbol{n}(s)$ is the internal force vector carried by the needle, parallel to the needle path toward the needle's tip, and representing the transfer of $\boldsymbol{F}_{\text{ins}}$ to $\boldsymbol{F}_p$. The inset in Fig. 3 shows the $\boldsymbol{n}(s)$ vector is the force that the proximal

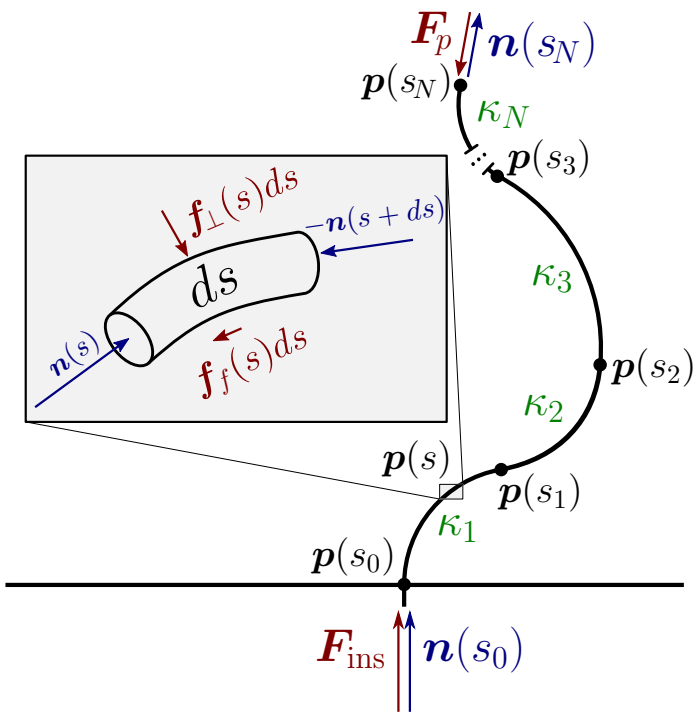


Fig. 3. An example piecewise-circular arc path with parameter endpoints $s_i$ and curvatures $\kappa_i$. A small segment of length $ds$ is shown with forces. Position $\boldsymbol{p}(s)$, friction $\boldsymbol{f}_f(s)$, tissue normal force $\boldsymbol{f}_\perp(s)$, internal needle force $\boldsymbol{n}(s)$, insertion force $\boldsymbol{F}_{\text{ins}}$, and piercing force $\boldsymbol{F}_p$ are labeled.

material exerts on the distal material. Dividing by $ds$ and allowing $ds \to 0$, then

$$-\dot{\boldsymbol{n}}(s) + \boldsymbol{f}_\perp(s) - f_f(s)\dot{\boldsymbol{p}}(s) = 0, \tag{1}$$

where the dot represents the derivative with respect to $s$. This is the conventional Cosserat-string equilibrium equation,[30,41] with the distributed force separated into two orthogonal components. The assumption that the internal force vector $\boldsymbol{n}(s)$ is aligned with the tangent vector $\dot{\boldsymbol{p}}(s)$ implies that the needle cannot carry internal shear loads. Thus

$$\begin{aligned}\boldsymbol{n}(s) &= n(s)\dot{\boldsymbol{p}}(s)\\ \dot{\boldsymbol{n}}(s) &= \dot{n}(s)\dot{\boldsymbol{p}}(s) + n(s)\ddot{\boldsymbol{p}}(s),\end{aligned}$$

where the scalar $n(s) = \|\boldsymbol{n}(s)\|$ represents the compressive force carried by the needle shaft at $s$. Substituting these into (1) and decomposing into the parallel and perpendicular components, we get

$$\begin{aligned}\dot{n}(s) &= -f_f(s)\\ \boldsymbol{f}_\perp(s) &= n(s)\ddot{\boldsymbol{p}}(s).\end{aligned} \tag{2}$$

For any path-length parameterized curve $\boldsymbol{p}(s)$, the magnitude of $\ddot{\boldsymbol{p}}(s)$ is the curvature, $\kappa(s)$, thus

$$f_\perp(s) = \kappa(s)n(s), \tag{3}$$

where $f_\perp(s)$ is the magnitude of $\boldsymbol{f}_\perp(s)$.

### 3.1.3. *Friction Model and Force Integration*

To calculate $n(s)$, the magnitude at one point must be given. Typical points are either at the beginning (the insertion force $n(0) = F_{\text{ins}}$) or the end (the piercing force $n(L) = F_p$) as depicted in Fig. 3. For a given needle path, we consider a known piercing force magnitude, $F_p$. We assume the magnitude of the needle's insertion force, $F_{\text{ins}}$, is sufficiently large to overcome friction and provide the needed piercing force, $F_p$, at the tip. However, it could be easily adapted to a known insertion force magnitude, $F_{\text{ins}}$, if that is measured or controlled, thus using the model to predict the current piercing force magnitude, $F_p$. In our evaluation, we assume a constant insertion speed and piercing force $F_p$.

We assume a kinetic friction model for $f_f(s)$ of the form

$$f_f(s) = \mu(s)\big(f_c(s) + f_\perp(s)\big), \tag{4}$$

where $\mu(s)$ is the conventional coefficient of kinetic friction, $f_\perp(s)$ is the needle shaft's normal force on the tissue, and $f_c(s)$ is the distributed compressive force of the surrounding squeezing tissue; $\mu(s)f_c(s)$ is the resulting nominal distributed frictional force that would be present even for a straight needle path. Substituting this friction model into (2), we arrive at the following first order linear differential equation

$$\dot{n}(s) = -\mu(s)f_c(s) - \mu(s)\kappa(s)n(s). \tag{5}$$

Solving this, subject to an initial or final condition, yields the internal compression force in the needle, from which the tissue normal force can be calculated via (3). In general, $f_c(s)$ and $\mu(s)$ could vary along $s$ as the needle passes through heterogeneous tissues; $F_p$ may vary for each intermediate needle shape through heterogeneous tissue or tissue state. Additionally, $\mu(s)$ and $F_p$ may depend on the rotational velocity of the needle.[26] We can numerically integrate (5) backward from the tip to the base starting with $n(L) = F_p$, and substitute the solution into (3) to calculate the tissue normal force distribution along the needle's path. Alternatively, we can also express the general solution for $n(s)$ as

$$\begin{aligned}n(s) &= Ae^{-B(s)} - e^{-B(s)}\int \mu(s)f_c(s)e^{B(s)}ds\\ B(s) &= \int \mu(s)\kappa(s)ds,\end{aligned}$$

where $A$ is a constant of integration that can be determined by applying the tip condition $n(L) = F_p$, and where, depending on the nature of the functions $f_c(s)$, $\mu(s)$, and $\kappa(s)$, the integrals can either be evaluated analytically or numerically.

If $f_c(s)$, $\mu(s)$, and $\kappa(s)$ are piecewise constant—say $f_{c,i}$, $\mu_i$, and $\kappa_i$ on $s \in (s_{i-1}, s_i)$ as in Fig. 3, and let $n_i(s) = n(s)$ and $f_{\perp,i}(s) = f_\perp(s)$ for the $i^{\text{th}}$ segment—then for $s \in (s_{i-1}, s_i)$, and $\kappa_i > 0$, the solution reduces to

$$n_i(s) = -\frac{f_{c,i}}{\kappa_i} + \left(n_{i+1}(s_i) + \frac{f_{c,i}}{\kappa_i}\right)e^{\mu_i\kappa_i(s_i - s)}, \tag{6}$$

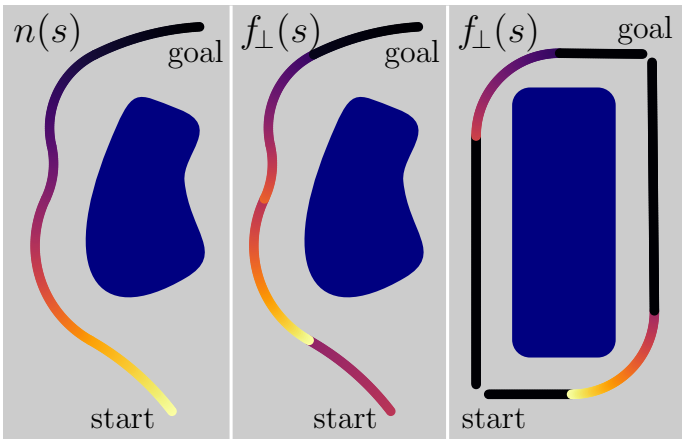


Fig. 4. Force heat maps along the needle path using this work's new tissue normal force model. Darker colors indicate small values, lighter colors indicate large values. **(a)** Internal compression force $n(s)$ carried by the needle from insertion to tip piercing force. **(b)** Resulting magnitude of the normal force exerted from the needle on the tissue $f_\perp(s)$ for the same path followed in (a). **(c)** Two paths from start to goal of the same length and of the same two straight segments and one arced segment. This demonstrates that high curvature at the path's beginning rather than its end results in much higher tissue normal forces; in this case, the lower-right's max $f_\perp(s)$ is 74% higher than in the upper-left.

with (3) becoming

$$f_{\perp,i}(s) = \kappa_i n(s).$$

For zero-curvature sections, $\kappa_i = 0$, $f_{\perp,i}(s) = 0$, and $n_i(s) = n_{i+1}(s) + \mu_i f_{c,i}(s_i - s)$. This solution can be iteratively evaluated section by section, starting at $s_i = L$ and proceeding backward. Note that the $n(s)$ solution is continuous across the entire needle trajectory, whereas $f_\perp(s)$ is discontinuous due to possible curvature discontinuities at each $s_i$, as illustrated in Fig. 4(a) and 4(b) respectively.

If we choose to ignore the effects of friction (by setting $\mu(s) = 0$), we get $f_\perp(s) = \kappa(s)F_p$, which results in a tissue normal force directly proportional to the curvature. Thus, while it may be intuitive to assume the curvature itself would be a good proxy for the probability of tissue compression or shearing, our model predicts that assumption is only true in the absence of shaft-to-tissue friction. If we ignore the influence of $f_\perp(s)$ on friction (by removing $f_\perp(s)$ from (4), assuming $f_\perp(s) \ll f_c(s)$), we get a simple linear internal force model for (5) with friction being independent of needle shape. If we consider the full friction model, even for a small friction coefficient $\mu_i$, the required insertion force for a given piercing force grows exponentially with the product of the friction coefficient, length, and curvature. As the path gets longer, the internal needle force, $n(s)$, grows exponentially as seen in (5), thus predicting a sharp increase in the tissue-damage probability.

#### 3.1.4. *Friction Models*

In this work, we consider friction models that consist of constant $f_c$, $\mu$, and $F_p$ over the full needle shape.

The first friction model we consider ignores the relation of the needle rotational velocity on friction behavior, and uses the same $f_c$, $\mu$, and $F_p$ for the full insertion trajectory. We call this the *single-parameter* model in our evaluation.

Because of the observation that insertion force decreases with needle rotation,[26] we consider a second friction model that utilizes separate $\mu$ and $F_p$ parameters for when the needle is rotating or non-rotating. We assume the compressive tissue force $f_c$ is unaffected by needle rotation, and therefore, this second friction model uses a single $f_c$ regardless of the needle rotational velocity. We call this the *double-parameter* model in our evaluation.

To clarify, when the needle is rotating, the needle tip moves in a straight path. When the needle is non-rotating, the needle tip moves in a constant curvature arc in the direction of the bevel tip, specifically at the maximum curvature $\kappa_{\max}$. To achieve curvature between 0 and $\kappa_{\max}$, we employ duty cycling between rotating and non-rotating states proportional to the desired percentage of $\kappa_{\max}$ curvature.[13,42,43] Although rotating and non-rotating sections dictate the needle tip's path, when the needle is rotating, the rotating friction coefficient, $\mu_{\text{rot}}$, applies to the entire path; likewise for the non-rotating friction coefficient, $\mu_{\text{norot}}$.

#### 3.1.5. *Model Fitting*

Measuring the normal forces between the needle and tissue is difficult due to the challenge of instrumenting such thin tissue-embedded needles without interfering with the force interaction. However, a key insight of our work is that the model can be fit without such measurements. We present two fitting methods. The first method fits based on the axial insertion forces, which can be measured by instrumenting the needle outside of the tissue. However, this is itself also difficult as it is non-trivial to completely capture all forces at the needle insertion site while rotating the needle and constraining it from buckling in air. The second, and potentially less burdensome method, is to fit the model using a set of labeled shearing events.

When using measured insertion forces, $F_{\text{ins}}$, one may fit the model parameters using any non-linear least squares solver, fitting on the error in $F_{\text{ins}}$ between measured values and the model's prediction. Alternatively, if given an average shearing force $\bar{f}_{\text{shear}}$, our model can predict the depth of shearing by determining the earliest point during path execution that exceeds $\bar{f}_{\text{shear}}$ over a given trajectory. This strategy is the basis of our second fitting method; one may similarly fit the model parameters using any non-linear least squares solver, fitting on the error between the predicted and measured shearing depths.

For models fit against measured $F_{\text{ins}}$, the average shear force $\bar{f}_{\text{shear}}$ can be viewed as an additional model parame-

ter, and fit to labeled shearing depths. We use the dataset's sample mean of the model's predicted maximal $f_\perp(s)$ over the needle's shapes at the labeled shearing depths.

Given that we use these fit models exclusively as cost functions in motion-planning, the exact magnitude of predicted needle-tissue force need not be fully accurate. What matters is the model's ability to rank paths relative to each other, with the goal of generating trajectories with all $f_\perp(s)$ below the unknown minimum shearing threshold, $f_{\text{thresh}}$. To this end, we evaluate our models by comparing the ranking they assign to paths against the true ranking (from labeled shearing depths). Since path ranking is scale-invariant, the $\bar{f}_{\text{shear}}$ used in fitting against measured shearing depths is functionally arbitrary.

We use the Trust Region Reflective algorithm[44] for non-linear least squares. We constrain all parameters to be strictly positive to represent meaningful physical quantities. For the double-parameter model, we further constrain $F_{p,\text{rot}} \leq F_{p,\text{norot}}$ and $\mu_{\text{rot}} \leq \mu_{\text{norot}}$ to match the prior observation of lower insertion force during needle rotation.[26]

### 3.2. *Motion Planning*

We propose a motion-planning framework that enables planning of needle trajectories with a lower risk of tissue damage by minimizing the modeled normal forces being applied by the needle to the tissue during insertion, thus increasing the likelihood that $f_\perp(s) < f_{\text{thresh}}$ for all $s$.

#### 3.2.1. *Bottleneck Cost*

Let $\boldsymbol{\pi}$ be a needle trajectory parameterized by time, $t \in [0, t_f]$, with $t_f$ representing the final time of trajectory $\boldsymbol{\pi}$. Let $\boldsymbol{p}_t(s)$ be the needle's centerline curve, as defined in Section 3.1, at time $t$ of trajectory $\boldsymbol{\pi}$ (denoted $\boldsymbol{\pi}(t)$); likewise let the $t$ subscript refer to the associated function over the needle shape at $\boldsymbol{\pi}(t)$. We define our force-based cost as the maximal tissue normal force along any needle shape within the trajectory,

$$C_F(\boldsymbol{\pi}) = \max_{t\in[0,t_f]} \max_{s\in[0,L_t]} f_{\perp,t}(s),$$

with $f_{\perp,t}(s)$ determined by our force model above in (3).

This $C_F(\boldsymbol{\pi})$ cost function is an example of a bottleneck cost, a concept that has been extensively studied in the motion-planning community (see, e.g., from Solovey *et al.*[45] and references within) with diverse applications such as following manipulator and surgical trajectories.[46,47]

Formally, if $c$ is a point-wise cost along a trajectory $\boldsymbol{\pi}$, then we can construct its associated *bottleneck cost* as

$$C(\boldsymbol{\pi}) = \max_{t\in[0,t_f]} c(\boldsymbol{\pi}(t)).$$

Our point-wise trajectory cost $c_F$ (also referred to as the needle shape cost) is the maximal tissue normal force along the needle shape at time $t$,

$$c_F(\boldsymbol{\pi}(t)) = \max_{s\in[0,L_t]} f_{\perp,t}(s).$$

**Algorithm 1** Bottleneck-Cost Planner

1: **procedure** PLANNER($ALG$, $\boldsymbol{q}_0$, $G$, $O$, $C$, $\varepsilon$)
   $ALG$: sampling-based motion planner
   $\boldsymbol{q}_0$: start configuration  $G$: goal configuration set
   $O$: obstacle set  $C$: cost function
   $\varepsilon$: approximation parameter
2: $c_{\max} \leftarrow \infty$
3: **while** *time allows* **do**
4: $\boldsymbol{\pi} \leftarrow ALG(\boldsymbol{q}_0, G, O, C, c_{\max})$
5: $c_{\max} \leftarrow C(\boldsymbol{\pi})/(1+\varepsilon)$
6: **report** $\boldsymbol{\pi}$

We use the common follow-the-leader assumption: the needle shape at $\boldsymbol{\pi}(t)$ is equal to the needle tip trajectory from 0 to $t$; i.e., if $t < t'$ and $s \in [0, L_t]$, then $\boldsymbol{p}_t(s) = \boldsymbol{p}_{t'}(s)$. In the case of constant model parameters during the trajectory, the maximal shape cost is at the trajectory's end, $\boldsymbol{\pi}(t_f)$. However, in that case, our cost $C_F$ maximizes over the needle shape and resembles a bottleneck cost.

One key property of bottleneck costs is that a trajectory's cost is the max of its subtrajectories' costs, i.e., if $t_1 < t_2 < t_3$, then

$$C(\boldsymbol{\pi}[t_1, t_3]) = \max(C(\boldsymbol{\pi}[t_1, t_2]), C(\boldsymbol{\pi}[t_2, t_3]));$$

whereas accumulation-based costs are additive,

$$C(\boldsymbol{\pi}[t_1, t_3]) = C(\boldsymbol{\pi}[t_1, t_2]) + C(\boldsymbol{\pi}[t_2, t_3]).$$

Existing optimizing motion planners either (i) require solving the two-point boundary value problem (see, e.g.,[45,48,49]) or (ii) cannot use a bottleneck cost.

#### 3.2.2. *Approach*

As we are not aware of any existing method to efficiently solve the two-point boundary value problem for steerable needles, we introduce a general simple-yet-effective framework. Our approach, summarized in Alg. 1, takes as input any sampling-based motion planner $ALG$ that can efficiently discard candidate paths below a given cost threshold $c_{\max}$ during its search, such as discarding edges that cause the path's cost to exceed $c_{\max}$.[a] Our algorithm also requires an approximation factor $\varepsilon$, which controls how aggressively the cost threshold geometrically decreases after each successive found candidate trajectory. For the first solution to be unconstrained, we initialize $c_{\max}$ to infinity (Alg. 1 line 2). Once a solution is obtained, the maximal cost value $c_{\max}$ is updated to be $C(\boldsymbol{\pi})/(1+\varepsilon)$ (Alg. 1 line 5), where $C$ is the cost function and $\boldsymbol{\pi}$ is the solution returned by $ALG$ (Alg. 1 line 4).

If $c^*$ is the optimal cost (i.e., $c^* = \inf_{\boldsymbol{\pi}} C(\boldsymbol{\pi})$), then no progress can be made if $c_{\max} < c^*$, in which case, the

[a]This is a very natural assumption; any planner that maintains paths using a configuration-space graph can typically be adapted to discard candidate paths below a given cost threshold.

previous plan would have cost $c = (1+\varepsilon)c_{\max} < (1+\varepsilon)c^*$. A large $\varepsilon$ may reach this point sooner than a small $\varepsilon$, but may ultimately find a final trajectory with higher cost.

#### 3.2.3. *Implementation*

To apply this proposed framework to our needle-steering domain, we use as $ALG$ the RG-RRT algorithm[39]—a state-of-the-art motion planner for needle steering. For our setting we make two changes to RG-RRT: (i) instead of planning from the needle-insertion site to the target in the body, we perform a backward search and plan from the target in the body to a specified insertion site, and (ii) if an edge under consideration would exceed the provided cost threshold $c_{\max}$, then we mark it as invalid.

The backward search is due to our choice of assuming a known constant piercing force $F_p$, and the model thus solving for the forces backward, as in (6). Because of the follow-the-leader assumption we only need to consider the final needle shape. If we have a piecewise-constant $F_p$, we would need to calculate the maximal force over all subshapes where the tip is at a piercing force discontinuity. This computation could be done as a single backward pass over the final shape, accounting for each individual subshape ending at piercing force discontinuity boundaries.

For constant piercing force $F_p$, we only need to consider the final shape when computing $f_\perp(s)$, which depends on $\kappa_i$ and $n(s)$ in (3). This is because a path extension can only increase $f_\perp(s)$, since $\kappa_i$ is a constant, but $n(s)$ grows exponentially. To compute $f_\perp(s)$ along a single needle shape, we start at the tip where $n(L) = F_p$, compute $n(s)$ backward one segment at a time using (6), and use (3) to compute $f_\perp(s)$. We store the internal needle force $n(s)$ as part of the motion-planning state, which, combined with planning from the goal toward the start, enables fast computation of $f_\perp(s)$ for each added segment. Each segment is checked against the maximum-allowed cost when added and pruned if that cost is exceeded (see $c_{\max}$ in Alg. 1 line 4). The resulting found plan from the goal to the start is then reversed to create a planned trajectory. Planning the path as if it were reversed in direction enables efficient and accurate computation of the maximum normal forces during forward insertion.

When considering the double-parameter model, our motion planner keeps track of two separate $n(s)$ values as it propagates from the needle tip to the base. A segment is considered rotating in our implementation if $\kappa \leq 0.9\kappa_{\max}$ and is non-rotating if $0.1\kappa_{\max} \leq \kappa$; for $0.1 \leq \frac{\kappa}{\kappa_{\max}} \leq 0.9$, the segment acts as both due to duty cycling.

## 4. Experiments

We first validate our force model's ability to rank candidate paths through physical experiments. We then use one set of fit parameters to compare the effectiveness of planning for needle steering with our force-based cost function (the force planner) compared to using the path-length cost (the length planner). We perform planning in 400 randomly generated environments. We compare the plans from the force and length planners by their path lengths and maximal tissue forces. Finally, we demonstrate the use of our force planner within a simulated lung biopsy scenario, planning through a segmented lung CT.

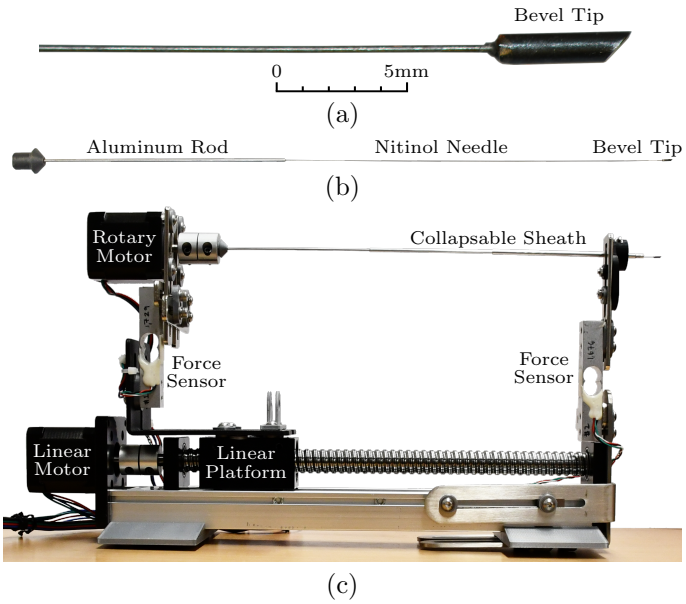


Fig. 5. The **(a)** needle bevel tip, **(b)** full needle, and **(c)** robot design for our physical experiments.

### 4.1. *Physical Experiment*

Our needle, shown in Fig. 5(b), consists of a nitinol tube with a large bevel tip (see Fig. 5(a)). The thin 165 mm flexible nitinol tube section has a 0.37 mm outer diameter (OD) and a 0.24 mm inner diameter (ID). The 5 mm bevel tip is 1.22 mm OD, 1.02 mm ID, filled with cyanoacrylate, and beveled to approximately 45°. For stability and extra length to account for the collapsed sheath, the thin nitinol tube is affixed to a 107 mm aluminum rod.

The robot, shown in Fig. 5(c), uses two Nema 17 stepper motors, one for linear actuation, and the other to rotate the needle. A two-segment collapsible sheath prevents the needle from buckling in air.[27] The sheath and rotary motor are affixed to 1 kg 1-D strain-gauge force sensors. We add both force signals to measure the needle's axial force.

Our phantom is 10% Knox gelatin and 90% water, by weight. Above the gelatin, a camera records insertions for later labeling of curvature and shearing (see Fig. 2).

We insert the needle at 5 mm/s in open-loop control. The needle's rotational velocity alternates between 0 and 2 rev/s. We achieve variable curvature using duty cycling.[42]

#### 4.1.1. *Results*

We gathered 35 individual runs on a wide variety of controlled paths. Each path is 150 mm, but we stop insertion when we observe shearing. All paths start with a straight segment (i.e., the needle rotating) from between 10 mm to 100 mm. Of the 35 paths, 19 of them contained at least one duty-cycled segment from 70 to 95%. Before beginning a run, the needle is inserted 1 to 2 mm manually and adjusted until the force sensor readings are nearly at zero.

To perform a fit and generate predictions from our model, we require the path curvature at each point. On 13 paths, we labeled the change in orientation $\Delta\theta$ from video footage and controlled insertion length $\Delta s$, which results in $\kappa = {}^{\Delta\theta}/_{\Delta s}$. We estimated an average $\kappa_{\max} = 0.020\,\mathrm{mm}^{-1}$ and standard deviation $0.003\,\mathrm{mm}^{-1}$ (turning radius of 50 mm). We use $\kappa_{\max} = 0.02\,\mathrm{mm}^{-1}$ in all fitting and planning in this paper.

For brevity, we refer to the single- and double-parameter models fit from measured $F_{\text{ins}}$ as Force-Single and Force-Double, respectively. We likewise define Shear-Single and Shear-Double as the models fit from labeled shearing depths. When fitting against shear depth, we use a constant $\bar{f}_{\text{shear}} = 17.6\,\mathrm{mN/mm}$, calculated from the mean between many average thresholds from fits against insertion force. We chose this value to enable the two fit models to scale similarly.As the ranking is scale-invariant, this value has no impact on the models' path rankings.

To evaluate each model's ability to rank paths, we order the paths by shearing depth, comparing manually labeled shearing depths against the model predictions. The Kendall's $\tau$ correlation is a statistical measure of the similarity of two ordered sets, commonly used in information retrieval and recommender systems.[50] We use the similarity-weighted Kendall $\tau$ distance,[50] a generalization of Kendall's $\tau$ weighted by element distances,

$$K_D = \sum_{i<j} D_{ij}\sigma_{ij},$$

where $\sigma_{ij}$ is one if elements $i$ and $j$ are out of order and $D_{ij}$ is their distance; i.e., the absolute difference between the actual shear depths. The Kendall correlation coefficient is obtained from the Kendall distance by normalizing, inverting, and scaling to be between -1 and 1,

$$\tau_D = 2 - \frac{K_D}{\sum_{i<j} D_{ij}}.$$

To obtain a $p$-value, we use the law of large numbers and a null hypothesis of random ordering. Using this similarity-weighted Kendall $\tau_D$, we can measure the quality of path rankings such that misranked paths result in a metric distance proportional to the difference between their measured shearing depths.

To determine the effect of the model fitting dataset size on the ranking capability of our four models, we compare the obtained $\tau_D$ for various fitting dataset sizes in Fig. 6.

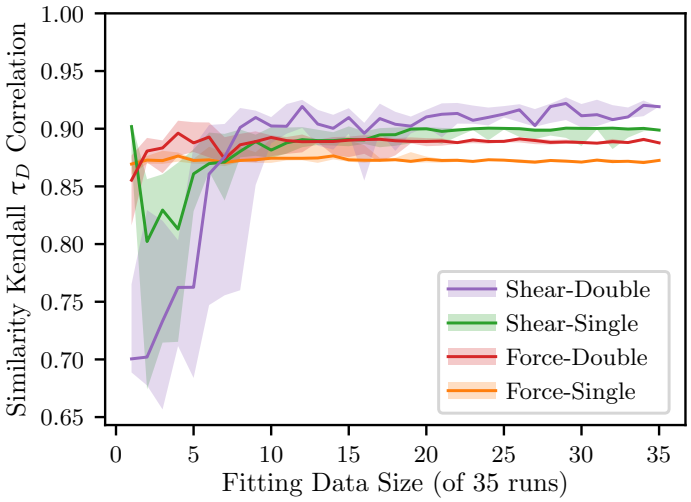


Fig. 6. Fitting data size versus similarity Kendall $\tau$ correlation coefficient. For each fitting data size, $d$, we created ten random samplings and performed fits. We show the median $\tau_D$ with a solid line between upper and lower quartiles in the shaded regions. A perfect ordering is correlation 1 and a random ordering in expectation is correlation 0.

For each dataset size, $d$, we made ten samplings of $d$ runs for fitting, with the remainder kept as a hold-out dataset. All 35 runs are used in calculating $\tau_D$. The Force-Single, Force-Double, Shear-Single, and Shear-Double models converge to a median $\tau_D$ of 0.87, 0.89, 0.91, and 0.92, respectively; with $p$-values between $1.5 \times 10^{-7}$ to $5.8 \times 10^{-7}$. The Force-Single, Force-Double, and Shear-Single appear to converge after a dataset size of 2, 10, and 18, respectively. The Shear-Double model shows higher variability, but roughly converges at a dataset size of 20. The $F_{\text{ins}}$-fit models converge much sooner, primarily due to the large number of force samples (approximately 100 to 300 samples per run), compared to a single shearing-depth sample per run. But the shear-depth-fit models perform better in ranking, primarily because the ranking is also performed on shearing depth. We also see the double-parameter models can fit better than single-parameter models but require more data. However, we show that all fit models provide similar discriminatory abilities, some of which require significantly fewer experimental runs to fit well.

For the remainder of the paper, we use fits from one of the random datasets of size 12 discussed previously. The fit model parameters are seen in Table 1. We note that the parameters vary quite heavily between the models. The Shear-Single and Shear-Double models are only expected to accurately predict shearing depth, not specific force values; therefore, their fit parameters may exhibit large variance. The primary difference between Shear and Force model parameters is the predicted friction coefficient, with the force-fit models predicting very small friction and the shear-fit models predicting very high friction. Of note, the 10 different fits of 12 runs varied widely in

Table 1. Fit parameters and $\tau_D$ correlation against 12 runs for our two models and two fitting strategies.

| Model | $F_{p,\text{rot}}$ (mN) | $F_{p,\text{norot}}$ (mN) | $\mu_{\text{rot}}$ | $\mu_{\text{norot}}$ | $\mu_{\text{rot}} f_c$ (mN/mm) | $\mu_{\text{norot}} f_c$ (mN/mm) | $\bar{f}_{\text{shear}}$ (mN/mm) | $\tau_D$ | $p$-value |
|---|---|---|---|---|---|---|---|---|---|
| Force-Single | 122.0 | 122.0 | 0.0371 | 0.0371 | 9.48 | 9.48 | 13.2 | 0.87 | $5.9 \times 10^{-7}$ |
| Force-Double | 123.5 | 123.5 | 0.000258 | 0.000276 | 9.27 | 9.98 | 13.1 | 0.89 | $3.6 \times 10^{-7}$ |
| Shear-Single | 438.5 | 438.5 | 0.287 | 0.287 | 4.99 | 4.99 | 17.6 | 0.90 | $2.3 \times 10^{-7}$ |
| Shear-Double | 82.8 | 171.4 | 0.232 | 0.248 | 11.07 | 11.83 | 17.6 | 0.94 | $0.7 \times 10^{-7}$ |

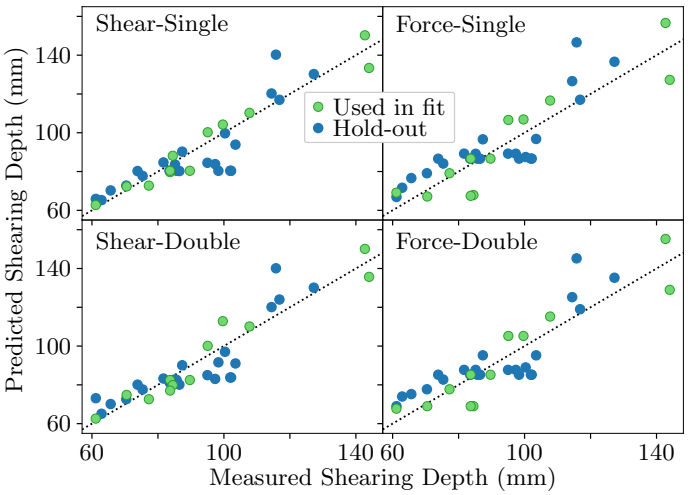


Fig. 7. Qualitative correlation visualization of measured shear depth versus predicted shear depth for various fits. The model parameters are fit from the same set of 12 randomly selected runs, shown in light green, with the remaining 23 runs shown in blue. A perfect model would have all points on the $y = x$ diagonal dotted line.

fit parameters, but their ability to accurately rank paths was not drastically impacted. For example, the $\mu_{\text{rot}}$ parameter had a median fit (with lower and upper quartiles specified with "Q:") of 0.019 (Q: 0.0001 to 0.13), 0.0003 (Q: 0.0001 to 0.12), 0.30 (Q: 0.04 to 0.61), and 0.33 (Q: 0.30 to 0.36) for Force-Single, Force-Double, Shear-Single, and Shear-Double, respectively, yet their $\tau_D$ correlations were 0.871 (Q: 0.870 to 0.888), 0.889 (Q: 0.876 to 0.896), 0.905 (Q: 0.902 to 0.908), and 0.920 (Q: 0.907 to 0.927), respectively over all 35 runs.

In Fig. 7, we demonstrate the correlation between measured and predicted shear depths of our four fit models. For a motion-planning cost function, it is more important that the correlation points are ordered (i.e., increasing) rather than lying along the diagonal $y = x$. For all four models, we qualitatively see a strong correlation between measured and predicted shear depths.

To demonstrate the fit quality and visualize our model's predicted forces, we display measured forces compared against predictions from the fit Force-Single and Force-Double models in Fig. 8(a) and Fig. 9(a) (for one run from the fit dataset and the hold-out set, respectively). The double-parameter model is able to account for jumps in the insertion force when the needle changes its rotational velocity. However, the errors (middle plot), predicted tissue force profiles (Fig. 8(b) and Fig. 9(b)), and predicted shearing depths (vertical lines in plots) of both models are very similar. Although the force fit is worse against the hold-out run than the in-fit run, the final predicted shearing depth is better in this particular hold-out example.

We briefly compare the predicted and measured insertion forces. The root mean square error (RMSE) of insertion force until shearing was 62 mN, 61 mN, 193 mN, and 166 mN for Force-Single, Force-Double, Shear-Single, and Shear-Double, respectively. These models show poor accuracy for insertion force. This is likely due to our assumption of negligible bending stiffness. However, these models can accurately rank paths, which can be leveraged as a useful motion-planning cost.

### 4.2. *Motion-Planning Evaluation*

As our method is the first to consider maximal tissue normal force, we evaluate our motion planning algorithm (Alg. 1) with our force-based cost function (using the Shear-Double model parameters from Table 1) versus the popular path-length cost. We refer to the planners that minimize path length and our force cost as the length planner and force planner, respectively.

We set a timeout of 100 s and an approximation factor $\varepsilon = 0.0001$. We implement random restarts if no solution is found after 10,000 RG-RRT iterations (i.e., number of sampled needle tip positions), increasing this limit by 5% each time we perform a random restart. On each run, both planners are provided the same random seed, ensuring their first solutions are identical before path optimization begins.

As shown in Fig. 10, we task the planner with finding a path in 3-D from the start to the goal, where the planner must avoid spherical obstacles. We evaluate the length and force planners in 400 environments with randomly generated spherical obstacles, using a needle of 1 mm OD and a minimum clearance of 1 mm. The start position and goal pose are identical and fixed for all environments. We generate the spherical obstacles with the radius sampled uniformly from 2 to 10 mm and the center sampled uniformly from the workspace. Spheres are rejected if they contain the start or goal positions. We generate these environments

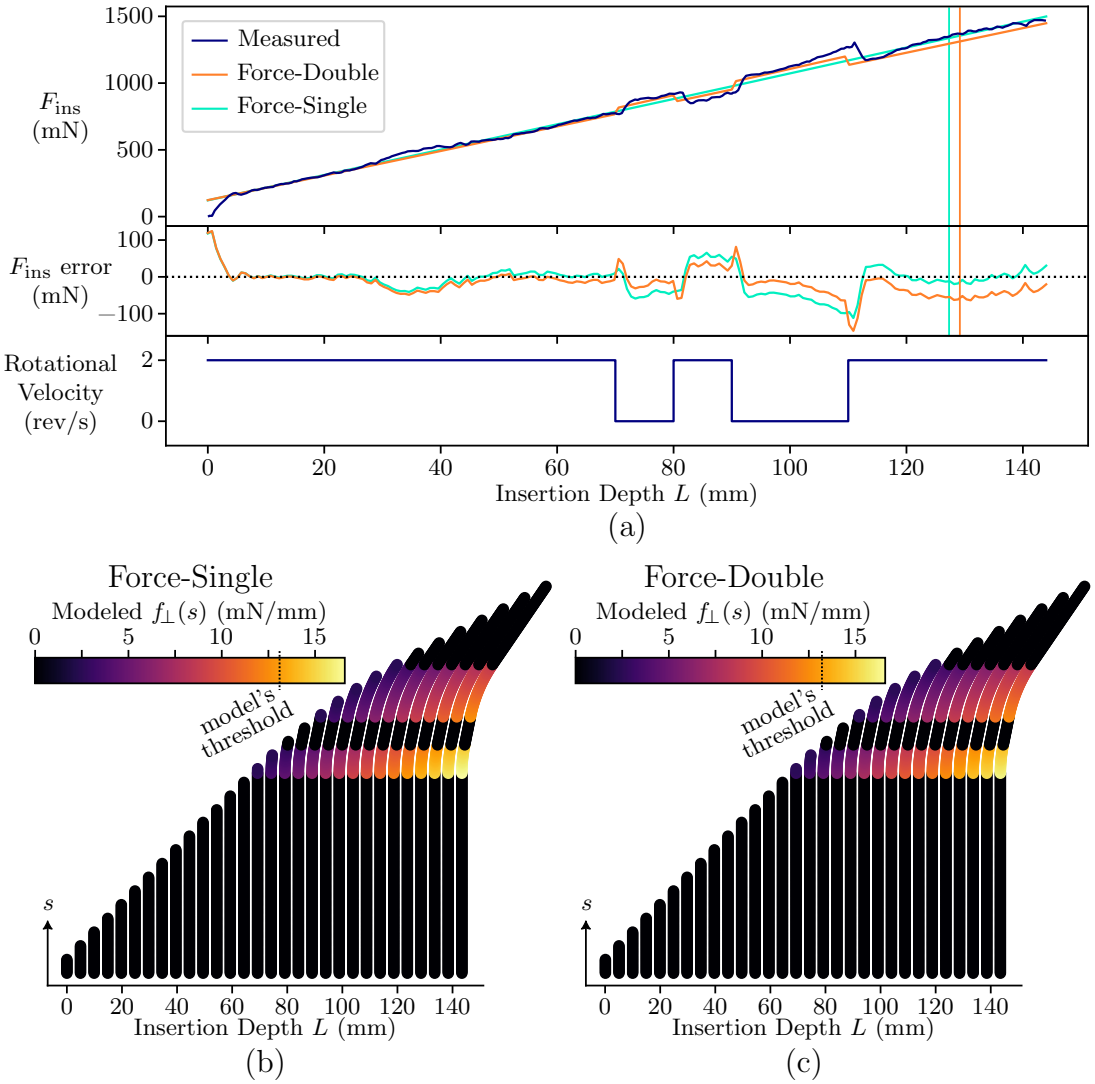


Fig. 8. Modeled and measured $F_{\text{ins}}$ of a run used in fitting, and the models' predicted tissue force along the path. **(a)** Plot of (top) measured and modeled $F_{\text{ins}}$, (middle) modeling error in $F_{\text{ins}}$, and (bottom) needle rotational velocity. The plot ends at the measured shearing, and the predicted shearing is indicated with vertical lines. The upward jumps in insertion force happen when the needle stops spinning, as seen in the rotational velocity subplot. **(b)** and **(c)** Intermediate needle shapes and modeled tissue force from Force-Single and Force-Double, respectively.

with at least four spheres, then continue adding spheres while the trivial motion-planning solution is collision-free. The trivial solution is a single constant-curvature path between the start and goal.

#### 4.2.1. *Results*

Our planner successfully found a plan in 331 of the 400 randomly generated environments. Since our environment generation does not ensure the existence of a solution, we discard from our analysis the 69 environments with no successful motion plans.

One example environment is demonstrated in Fig. 10. The initial path found by both planners (Fig. 10(a)) is suboptimal in both path-length and force costs. The subsequent paths found by the length planner (Fig. 10(b)) and the force planner (Fig. 10(c)) show a similarly obtained path length (difference of 0.2%), but the length planner's path shows significantly more curving near the start (see Fig. 10(d)), which results in 5.7 times higher force cost than the force planner's force cost.

As further evidence that the length cost function does not adequately minimize forces, the length planner's returned force costs after 100 s are $1.6 \pm 1.9$ times larger than those from the force planner (i.e., a force ratio of $2.6 \pm 1.9$). In Fig. 11, the quantile plot in the upper-left shows that at

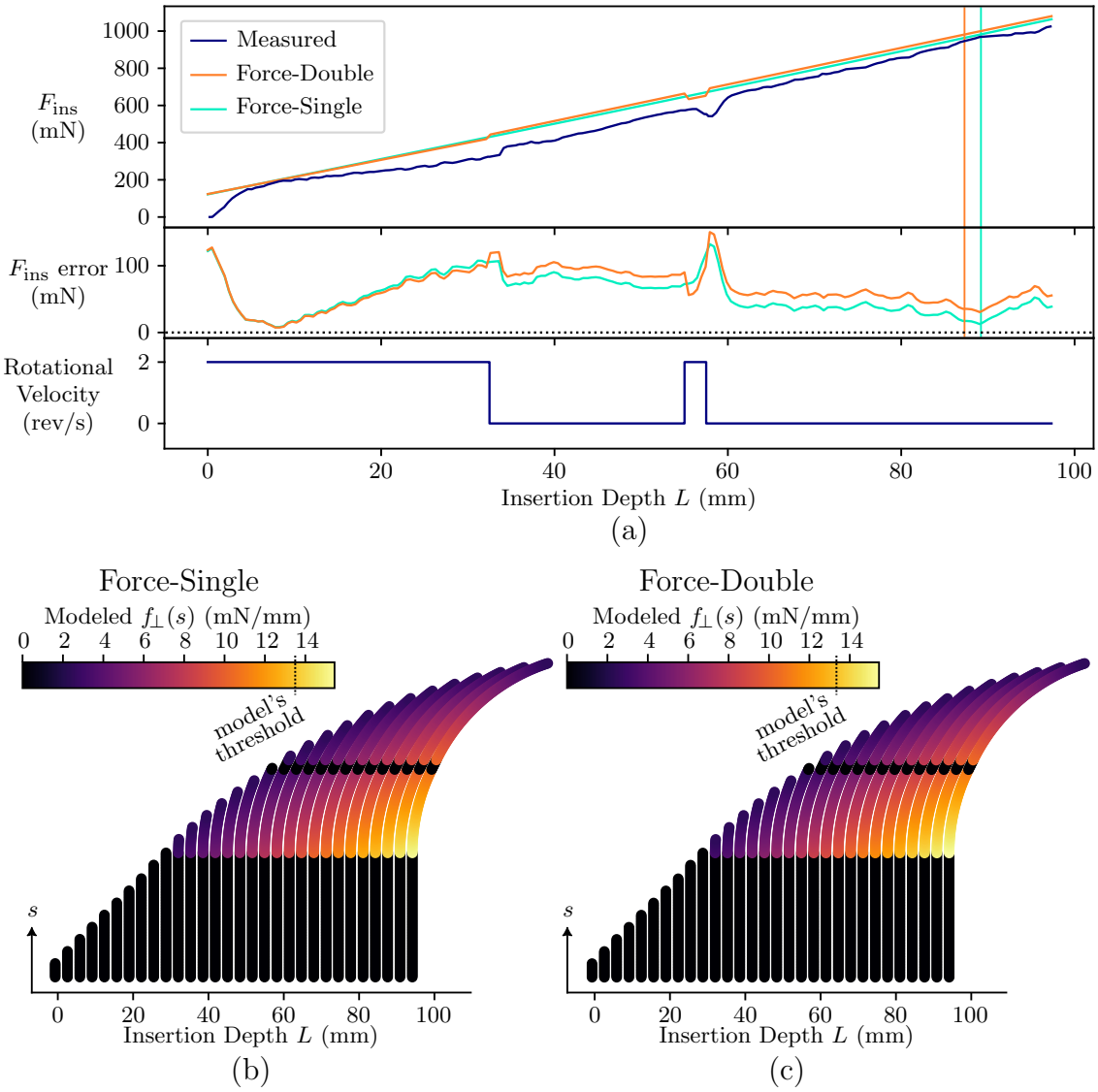


Fig. 9. Modeled and measured $F_{\text{ins}}$ from a hold-out run, and the models' predicted tissue force along the path. This plot is structured the same as Fig. 8, but shows a path not used in the fit. In this example, the predicted insertion forces from this particular fit do not fit the exponential behavior shown in the measured insertion force. Despite this insertion force mismatch, the predicted shearing depth for the Force-Double has nearly identical error percentage compared to Fig. 8 (10%), and for the Force-Single, the error percentage is much better (12% versus 4%).

around 10 s, over 90% of the returned paths have a larger force than those returned from the force planner. The top-right density plot in Fig. 11 additionally shows a large spread of force cost ratios after 100 s of planning and shows many plans that exhibit up to ten times the force cost than the force planner.

We also compare the path lengths over time for each of the planners. Notably, the force planner produces paths of comparable length to the length planner, but does so indirectly (see (6)) while significantly improving the tissue forces of the paths. Fig. 11 shows the length planner performs slightly better than the force planner in path length. The length cost ratio between the force-planner and length-planner is on average 1.0007 with standard deviation 0.0065 ($p$-value of 0.03 against the null hypothesis of 1.0 mean). This difference is imperceptible and well within the standard deviation of path lengths from the length planner (1.0%). This shows that optimizing for tissue forces enables found paths with drastically less force on surrounding tissue without measurably sacrificing in path length.

It is an intuitive result that a planner optimizing for tissue normal forces would produce plans that have lower tissue normal forces than one that was not. However we present this analysis to demonstrate that path length is

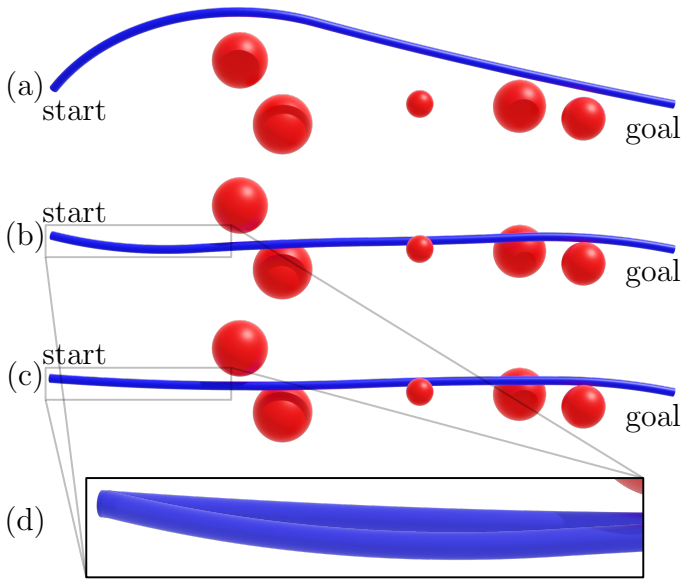


Fig. 10. Generated collision-free trajectories in a randomly generated 3-D environment with spherical obstacles. We compare paths generated by two cost functions: path-length cost and our method's force-based cost. **(a)** Initial solution by both planners before optimization. **(b)** and **(c)** Converged solutions from using the path-length and our force-based costs, respectively. Based on an average shearing threshold $\bar{f}_{\text{shear}} = 17.6\,\text{mN/mm}$ (from which this model was fit), the maximum modeled tissue forces for (a), (b), and (c), respectively, are 2.7, 1.1, and 0.2 times the threshold $\bar{f}_{\text{shear}}$. **(d)** 3× zoomed-in view of both solutions at the start; the path from (b) is below and (c) is above, with much more curvature on path (b). The length difference between (b) and (c) is less than 0.2%, but the force cost from (b) is 5.7 times larger than the force cost from (c).

not a sufficient proxy metric for tissue normal forces, even though path length has an impact on tissue normal forces as shown in (6). The intuition for this is shown in Fig. 4(c). Trajectories that are identical both in length and maximum curvature can have dramatically different maximum tissue normal forces. This highlights the need for considering the tissue normal forces explicitly during motion-planning.

### 4.3. *Anatomical Environment*

We next demonstrate initial feasibility of using the motion-planning method that considers tissue normal forces with a clinically relevant task in an anatomical environment. We task the motion planner with planning a path for a needle from a patient's chest wall to a target deep in the lung, as in percutaneous lung tumor biopsy. We utilize a CT scan from the 2017 lung CT segmentation challenge[51,52] in the cancer imaging archive.[53] Using the segmentation method of Fu *et al.*[9] we segment the large vasculature and bronchial trees in the lung. These are used as obstacles for the motion planner that must be avoided.

We ran the force and length planners on this problem 100 times with a timeout of 100 seconds each. We show in Fig. 12 one example plan from our force planner; demonstrating its ability to find a path from the start to the goal while avoiding the obstacles and doing so while minimizing tissue normal forces. The length planner's force cost was $(4 \pm 23)\%$ larger than the force planner's force cost, yet the force planner's length cost was only $(0.02 \pm 0.49)\%$ larger than the length planner's length cost.

## 5. Conclusion

This work provides the following contributions: (i) a simple and efficient Cosserat-string-based needle-to-tissue force and friction model, (ii) a clinically motivated and computationally efficient motion-planning cost function for needle steering based on our needle-to-tissue force and friction model, and a motion-planning algorithm that leverages our force-based cost function, and (iii) two effective strategies for fitting our force model parameters with easily obtained insertion force measurements or labeled shearing events, depending on whichever is easier to obtain. Minimizing the tissue normal forces during needle steering has the potential to significantly reduce the risk of critical tissue damage events, thus improving patient outcomes.

In this work, we utilized a homogeneous gel phantom to validate and fit our force model. In future work, we intend to utilize real heterogeneous tissues involved in clinical procedures to evaluate our method's efficacy in real clinical settings. Shearing events utilized in the model fitting process would then need to be measured in ex vivo tissue using medical imaging, such as fluoroscopy.

This work's analysis does not yet consider the stochasticity in needle control[54] and in damage outcome. We intend to investigate the use of our cost function in stochastic risk metrics for risk-based planning under uncertainty.[55]

## Acknowledgments

The authors would like to thank Ron Alterovitz and his group for their insights and assistance with segmentation, and Robert J. Webster III and his group for insights and valuable discussions.

This research was supported in part by the U.S. National Science Foundation (NSF) under Awards IIS-1652588 (CAREER) and CMMI-2133027, by the Israeli Ministry of Science & Technology grants no. 3-16079 and 3-17385 and in part by the United States-Israel Binational Science Foundation (BSF) grants no. 2019703 and 2021643

## References

[1] N. Abolhassani, R. Patel and M. Moallem, Needle insertion into soft tissue: A survey, *Med. Eng. Phys.* **29** (May 2007) 413–431.

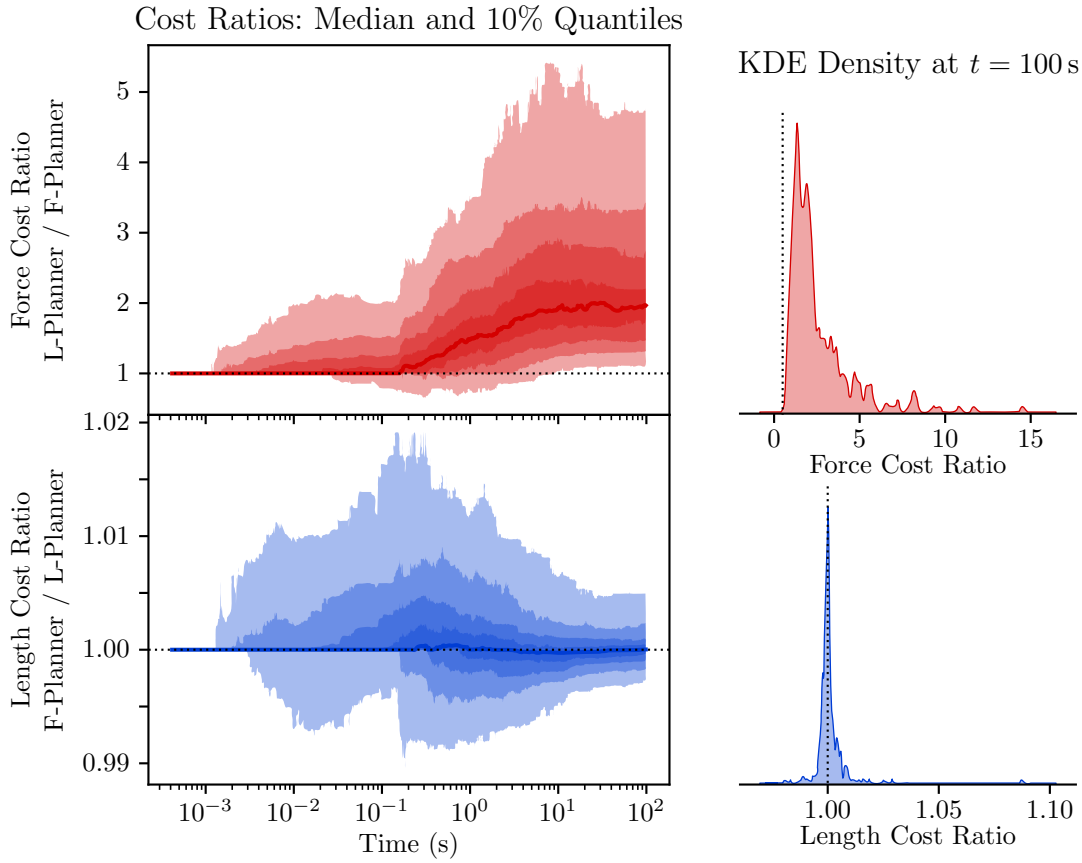


Fig. 11. From 331 random sphere environments, we compare the cost ratios of the length and force planners for both length and force costs versus planning time. (Top) The ratio of force costs with the length planner over the force planner, shown in red. A 1.0 ratio (shown as a dotted line) represents the force cost obtained from the force planner. (Bottom) The ratio of length costs with the force planner over the length planner, shown in blue. Likewise, the 1.0 line represents the length planner's achieved length cost. The ratios are generated pair-wise over plans for corresponding environments. (Left) We show the median (solid line) and four quantiles above and below (shaded) 10% quantile steps. (Right) We show the kernel-density estimate (KDE) of the cost ratios at 100 s.

[2] K. B. Reed, A. Majewicz, V. Kallem, R. Alterovitz, K. Goldberg, N. J. Cowan and A. M. Okamura, Robot-assisted needle steering, *IEEE Robot. Autom. Mag.* **18** (December 2011) 35–46.

[3] R. J. Webster, III, J. S. Kim, N. J. Cowan, G. S. Chirikjian and A. M. Okamura, Nonholonomic modeling of needle steering, *Int. J. Rob. Res.* **25** (May 2006) 509–525.

[4] M. Rox, M. Emerson, T. E. Ertop, I. Fried, M. Fu, J. Hoelscher, A. Kuntz, J. Granna, J. E. Mitchell, M. Lester, F. Maldonado, E. A. Gillaspie, J. A. Akulian, R. Alterovitz and R. J. Webster, III, Decoupling steerability from diameter: Helical dovetail laser patterning for steerable needles, *IEEE Access* **8** (October 2020) 181411–181419.

[5] N. J. van de Berg, D. J. van Gerwen, J. Dankelman and J. J. van den Dobbelsteen, Design choices in needle steering—A review, *IEEE/ASME Trans. Mechatron.* **20** (October 2014) 2172–2183.

[6] F. Yang, M. Babaiasl and J. P. Swensen, Fracture-directed steerable needles, *J. Med. Robot. Res.* **4** (March 2018).

[7] S. Patil, J. Burgner, R. J. Webster, III and R. Alterovitz, Needle steering in 3-D via rapid replanning, *IEEE Trans. Robot.* **30** (August 2014) 853–864.

[8] A. Kuntz, L. G. Torres, R. H. Feins, R. J. Webster, III and R. Alterovitz, Motion planning for a three-stage multilumen transoral lung access system, *2015 IEEE Int. Conf. Intell. Robots Syst. (IROS)*, Hamburg, Germany (September 2015), pp. 3255–3261.

[9] M. Fu, A. Kuntz, R. J. Webster, III and R. Alterovitz, Safe motion planning for steerable needles using cost maps automatically extracted from pulmonary images, *2018 IEEE Int. Conf. Intell. Robots Syst. (IROS)*, Madrid, Spain (October 2018), pp. 4942–4949.

[10] M. Pinzi, S. Galvan and F. Rodriguez y Baena, The adaptive Hermite fractal tree (AHFT): A novel surgical 3D path planning approach with curvature and heading constraints, *Int. J. Comput. Assist. Radiol.*

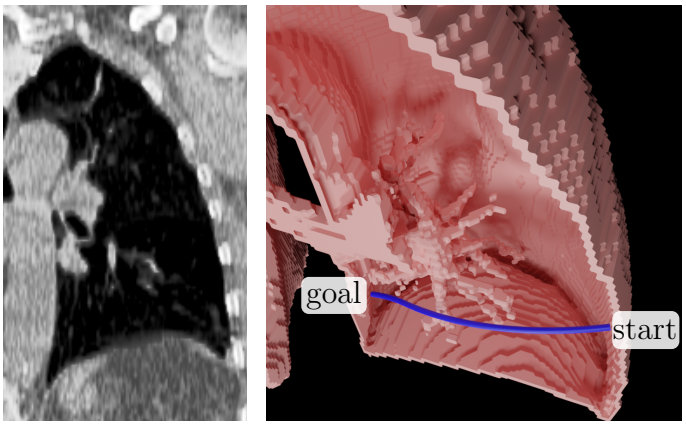


(a) (b)

Fig. 12. We demonstrate the feasibility of utilizing our force-based cost function in motion planning for a steerable needle in an anatomically relevant scenario. **(a)** The left lung from one slice of the used CT scan. **(b)** The segmented chest wall and bronchial tubes with a cutout for visualization. We show an example generated plan (blue) by our motion planner for a needle insertion site at the boundary of a patient's lung near the chest wall to reach a target deep in the lung. The plan curves around the lung's bronchial tubes while minimizing tissue normal forces.

*Surg.* **14** (April 2019) 659–670.

[11] A. Majewicz, S. P. Marra, M. G. van Vledder, M. Lin, M. A. Choti, D. Y. Song and A. M. Okamura, Behavior of tip-steerable needles in ex vivo and in vivo tissue, *IEEE Trans. Biomed. Eng.* **59** (October 2012) 2705–2715.

[12] R. Alterovitz, K. Goldberg and A. M. Okamura, Planning for steerable bevel-tip needle insertion through 2D soft tissue with obstacles, *Proc. 2005 IEEE Int. Conf. Robot. Autom.*, Barcelona, Spain (April 2005), pp. 1652–1657.

[13] D. Minhas, J. A. Engh and C. N. Riviere, Testing of neurosurgical needle steering via duty-cycled spinning in brain tissue in vitro, *2009 Annu. Int. Conf. IEEE Eng. Med. Biol. Soc.*, (September 2009), pp. 258–261.

[14] P. J. Swaney, A. W. Mahoney, B. I. Hartley, A. A. Remirez, E. Lamers, R. H. Feins, R. Alterovitz and R. J. Webster, III, Toward transoral peripheral lung access: Combining continuum robots and steerable needles, *J. Med. Robot. Res.* **2** (March 2017).

[15] J. A. Engh, G. Podnar, D. Kondziolka and C. N. Riviere, Toward effective needle steering in brain tissue, *2006 Int. Conf. IEEE Eng. Med. Biol. Soc. EMBC*, New York, NY, USA (September 2006), pp. 559–562.

[16] P. J. Swaney, J. Burgner, H. B. Gilbert and R. J. Webster, III, A flexure-based steerable needle: High curvature with reduced tissue damage, *IEEE Trans. Biomed. Eng.* **60** (November 2012) 906–909.

[17] V. K. Bui, S. Park, J.-O. Park and S. Y. Ko, A novel curvature-controllable steerable needle for percutaneous intervention, *Proc. Inst. Mech. Eng. Part H: J. Eng. Med.* **230** (August 2016) 727–738.

[18] G. Gerboni, J. D. Greer, P. F. Laeseke, G. L. Hwang and A. M. Okamura, Highly articulated robotic needle achieves distributed ablation of liver tissue, *IEEE Robot. Autom. Lett.* **2** (July 2017) 1367–1374.

[19] N. J. van de Berg, J. Dankelman and J. J. van den Dobbelsteen, Design of an actively controlled steerable needle with tendon actuation and FBG-based shape sensing, *Med. Eng. Phys.* **37** (June 2015) 617–622.

[20] L. Frasson, F. Ferroni, S. Y. Ko, G. Dogangil and F. Rodriguez y Baena, Experimental evaluation of a novel steerable probe with a programmable bevel tip inspired by nature, *J. Robot. Surg.* **6** (June 2012) 189–197.

[21] T. J. Schwehr, A. J. Sperry, J. D. Rolston, M. D. Alexander, J. J. Abbott and A. Kuntz, Toward targeted therapy in the brain by leveraging screw-tip soft magnetically steerable needles, *Proc. 14th Hamlyn Symp. Med. Robot. 2022*, London, UK (June 2022), pp. 81–82.

[22] M. Ilami, R. J. Ahmed, A. Petras, B. Beigzadeh and H. Marvi, Magnetic needle steering in soft phantom tissue, *Sci. Rep.* **10** (February 2020).

[23] A. Hong, A. J. Petruska, A. Zemmar and B. J. Nelson, Magnetic control of a flexible needle in neurosurgery, *IEEE Trans. Biomed. Eng.* **68** (February 2021) 616–627.

[24] N. Gessert, T. Priegnitz, T. Saathoff, S.-T. Antoni, D. Meyer, M. F. Hamann, K.-P. Jünemann, C. Otte and A. Schlaefer, Spatio-temporal deep learning models for tip force estimation during needle insertion, *Int. J. Comput. Assist. Radiol. Surg.* **14** (September 2019) 1485–1493.

[25] S. T. R. Gidde, A. Ciuciu, N. Devaravar, R. Doracio, K. Kianzad and P. Hutapea, Effect of vibration on insertion force and deflection of bioinspired needle in tissues, *Bioinspir. Biomim.* **15** (July 2020).

[26] R. Tsumura, Y. Takishita and H. Iwata, Needle insertion control method for minimizing both deflection and tissue damage, *J. Med. Robot. Res.* **4** (March 2019).

[27] R. J. Webster, III, J. Memisevic and A. M. Okamura, Design considerations for robotic needle steering, *Proc. 2005 IEEE Int. Conf. Robot. Autom.*, Barcelona, Spain (April 2005), pp. 3599–3605.

[28] M. Oldfield, D. Dini, G. Giordano and F. Rodriguez y Baena, Detailed finite element modelling of deep needle insertions into a soft tissue phantom using a cohesive approach, *Comput. Methods Biomech. Biomed. Engin.* **16** (May 2013) 530–543.

[29] B. Takabi and B. L. Tai, A review of cutting mechanics and modeling techniques for biological materials, *Med. Eng. Phys.* **45** (July 2017) 1–14.

[30] S. S. Antman, *Problems in Nonlinear Elasticity*, *Nonlinear Problems of Elasticity*, Applied Mathematical Sciences, Vol. 107 (Springer, New York, NY, USA,

2005), New York, NY, USA, ch. 14, pp. 513–584, second edn.

[31] O. Salzman, Sampling-based robot motion planning, *Commun. ACM* **62** (September 2019) 54–63.

[32] S. M. LaValle and J. J. Kuffner, Randomized kinodynamic planning, *Int. J. Rob. Res.* **20** (May 2001) 378–400.

[33] L. E. Kavraki, P. Švestka, J.-C. Latombe and M. H. Overmars, Probabilistic roadmaps for path planning in high-dimensional configuration spaces, *IEEE Trans. Robot. Autom.* **12** (August 1996) 566–580.

[34] J.-H. Yong and F. F. Cheng, Geometric Hermite curves with minimum strain energy, *Comput. Aided Geom. Des.* **21** (March 2004) 281–301.

[35] M. Fu, O. Salzman and R. Alterovitz, Toward certifiable motion planning for medical steerable needles, *Robot. Sci. Syst. XVII*, **2021**, Virtual (July 2021).

[36] M. Fu, K. Solovey, O. Salzman and R. Alterovitz, Resolution-optimal motion planning for steerable needles, *2022 Int. Conf. Robot. Autom. ICRA*, Philadelphia, PA, USA (May 2022), pp. 9652–9659.

[37] A. Favaro, L. Cerri, S. Galvan, F. Rodriguez y Baena and E. De Momi, Automatic optimized 3D path planner for steerable catheters with heuristic search and uncertainty tolerance, *2018 IEEE Int. Conf. Robot. Autom. ICRA*, Brisbane, QLD, Australia (May 2018), pp. 9–16.

[38] J. D. Gammell, S. S. Srinivasa and T. D. Barfoot, Batch informed trees (BIT*): Sampling-based optimal planning via the heuristically guided search of implicit random geometric graphs, *2015 IEEE Int. Conf. Robot. Autom. ICRA*, Seattle, WA, USA (May 2015), pp. 3067–3074.

[39] S. Patil and R. Alterovitz, Interactive motion planning for steerable needles in 3D environments with obstacles, *2010 3rd IEEE RAS EMBS Int. Conf. Biomed. Robot. Biomechatron.*, Tokyo, Japan (September 2010), pp. 893–899.

[40] S. W. Attaway, The mechanics of friction in rope rescue, *Int. Tech. Rescue Symp. ITRS 99*, **7**, Fort Collins, Colorado, USA (November 1999).

[41] D. C. Rucker and R. J. Webster, III, Statics and dynamics of continuum robots with general tendon routing and external loading, *IEEE Trans. Robot.* **27** (December 2011) 1033–1044.

[42] D. S. Minhas, J. A. Engh, M. M. Fenske and C. N. Riviere, Modeling of needle steering via duty-cycled spinning, *2007 29th Annu. Int. Conf. IEEE Eng. Med. Biol. Soc.*, Lyon, France (2007), pp. 2756–2759.

[43] Z. Qi, Q. Luo and H. Zhang, A tube-based robust MPC for duty-cycled rotation needle steering systems with bounded disturbances, *Trans. Inst. Meas. Control* **44** (February 2022) 960–970.

[44] M. A. Branch, T. F. Coleman and Y. Li, A subspace, interior, and conjugate gradient method for large-scale bound-constrained minimization problems, *SIAM J. Sci. Comput.* **21** (January 1999) 1–23.

[45] K. Solovey and D. Halperin, Efficient sampling-based bottleneck pathfinding over cost maps, *2017 IEEE Int. Conf. Intell. Robots Syst. (IROS)*, Vancouver, BC, Canada (September 2017), pp. 2003–2009.

[46] R. Holladay, O. Salzman and S. Srinivasa, Minimizing task-space Fréchet error via efficient incremental graph search, *IEEE Robot. Autom. Lett.* **4** (April 2019) 1999–2006.

[47] S. Niyaz, A. Kuntz, O. Salzman, R. Alterovitz and S. S. Srinivasa, Optimizing motion-planning problem setup via bounded evaluation with application to following surgical trajectories, *2019 IEEE Int. Conf. Intell. Robots Syst. (IROS)*, **2019**, Macau, China (November 2019), pp. 1355–1362.

[48] S. Karaman and E. Frazzoli, Sampling-based algorithms for optimal motion planning, *Int. J. Rob. Res.* **30** (June 2011) 846–894.

[49] O. Salzman and D. Halperin, Asymptotically near-optimal RRT for fast, high-quality motion planning, *IEEE Trans. Robot.* **32** (June 2016) 473–483.

[50] R. Kumar and S. Vassilvitskii, Generalized distances between rankings, *WWW '10 Proc. 19th Int. Conf. World Wide Web*, Raleigh, NC, USA (April 2010), pp. 571–580.

[51] J. Yang, H. Veeraraghavan, S. G. Armato III, K. Farahani, J. S. Kirby, J. Kalpathy-Kramer, W. van Elmpt, A. Dekker, X. Han and X. Feng, Autosegmentation for thoracic radiation treatment planning: A grand challenge at AAPM 2017, *Med. Phys.* **45** (October 2018) 4568–4581.

[52] J. Yang, G. Sharp, H. Veeraraghavan, W. van Elmpt, A. Dekker, T. Lustberg and M. Gooding, Data from lung CT segmentation challenge (version 3) [dataset] (May 2017), https://doi.org/10.7937/K9/TCIA.2017.3R3FVZ08.

[53] K. Clark, B. Vendt, K. Smith, J. Freymann, J. Kirby, P. Koppel, S. Moore, S. Phillips, D. Maffitt and M. Pringle, The cancer imaging archive (TCIA): Maintaining and operating a public information repository, *J. Digit. Imaging* **26** (July 2013) 1045–1057.

[54] W. Park, K. B. Reed, A. M. Okamura and G. S. Chirikjian, Estimation of model parameters for steerable needles, *2010 IEEE Int. Conf. Robot. Autom.*, Anchorage, AK, USA (January 2010), pp. 3703–3708.

[55] A. Majumdar and M. Pavone, How should a robot assess risk? Towards an axiomatic theory of risk in robotics, *Robot. Res. 18th Int. Symp. ISRR*, eds. N. M. Amato, G. Hager, S. Thomas and M. Torres-Torriti *Springer Proceedings in Advanced Robotics* **10**, (Springer Cham, Puerto Varas, Chile, d2020), pp. 75–84.